

# Ab initio prediction of strain-tunable spin defects in quasi-1D $\text{TiS}_3$ and $\text{NbS}_3$ nanowires

Jordan Chapman<sup>1</sup>, Arindom Nag<sup>2</sup>, Thang Pham<sup>2</sup>, and Vsevolod Ivanov<sup>1,3,4\*</sup>

<sup>1</sup>*Virginia Tech National Security Institute, Blacksburg, Virginia 24060, USA*

<sup>2</sup>*Department of Materials Science and Engineering, Virginia Tech, Blacksburg, Virginia 24061, USA*

<sup>3</sup>*Department of Physics, Virginia Tech, Blacksburg, Virginia 24061, USA and*

<sup>4</sup>*Virginia Tech Center for Quantum Information Science and Engineering, Blacksburg, Virginia 24061, USA*

Defects in atomically thin van der Waals materials have recently been investigated as sources of spin-photon entanglement with sensitivity to strain tuning. Unlike many two-dimensional materials, quasi-one-dimensional materials such as transition metal trichalcogenides exhibit in-plane anisotropy resulting in axis-dependent responses to compressive and tensile strains. Herein, we characterize the tunable spin and optical properties of intrinsic vacancy defects in titanium trisulfide ( $\text{TiS}_3$ ) and niobium trisulfide ( $\text{NbS}_3$ ) nanowires. Within our *ab initio* approach, we show that sulfur vacancies and divacancies ( $V_S$  and  $V_D$ , respectively) in  $\text{TiS}_3$  and  $\text{NbS}_3$  adopt strain-dependent defect geometries between in-plane strains of -3 % and 3 %. The calculated electronic structures indicate that both  $V_S$  and  $V_D$  possess in-gap defect states with optically bright electronic transitions whose position relative to the conduction and valence bands varies with in-plane strain. Further, our calculations predict that  $V_S$  in  $\text{TiS}_3$  and  $V_D$  in  $\text{NbS}_3$  exhibit transitions in their ground state spins; specifically, a compressive strain of 0.4 % along the direction of nanowire growth causes a shift from a triplet state to a singlet state for the  $V_S$  defect in  $\text{TiS}_3$ , whereas a tensile strain of 2.9 % along the same direction in  $\text{NbS}_3$  induces a triplet ground state with a zero-phonon line of 0.83 eV in the  $V_D$  defect. Our work shows that the anisotropic geometry of  $\text{TiS}_3$  and  $\text{NbS}_3$  nanowires offers exceptional tunability of optically active spin defects that can be used in quantum applications.

## INTRODUCTION

Color center defects in semiconductors are an attractive platform for applications in quantum information science [1, 2], as they couple light and electronic spin states, enabling scalable spin-photon qubit architectures [3]. Several promising defect candidates for spin qubits and single photon emitters (SPEs) have been realized in a number of bulk semiconductors including diamond, silicon carbide, and silicon [4–6], and more recently in two-dimensional (2D) materials [7, 8].

Strain engineering of color centers in semiconductor materials has been investigated as a strategy to tune the emission properties of atomic defects [9–12]. Low-dimension van der Waals (vdW) materials boast several distinct advantages over bulk materials for strain engineering of color center defects thanks to their atomically thin nature. Nanoscale vdW materials have been shown to exhibit drastically enhanced mechanical flexibility [13] compared to bulk counterparts, and their strains can be modulated via numerous methods, including attachment to an atomic force microscopy (AFM) cantilever [14], heating of gas molecules between layers [15], and bending of a substrate material [16]. Many 2D vdW materials, notably graphene, hexagonal boron nitride (hBN), and transition metal dichalcogenides (TMDCs), have been explored as hosts for strain-tunable quantum point defects [17]. For instance, strained defect SPEs within a single layer of tungsten diselenide [18] were found to exhibit narrow zero-phonon lines (ZPLs) of about 775 nm with widths measured at 75  $\mu\text{eV}$ , whereas single pho-

ton properties were not observed for unstrained defect structures. Density functional theory (DFT) calculations revealed that the observed emission peaks could not be attributed to a single defect (Se vacancy, W vacancy, or O interstitial [19]) and that the bright emission is likely due to the formation of a  $\text{WSe}_6$  pore vacancy. Negatively charged boron vacancy ( $V_B^-$ ) spin defects in hBN [20] are sensitive to strain [21], which has led to their use in quantum strain sensing applications [22, 23].

A family of materials related to TMDCs are transition metal trichalcogenides (TMTCs), which form quasi-one-dimensional (1D)  $\text{MX}_3$  nanowires ( $\text{M} = \text{Ti}, \text{Hf}$ , or  $\text{Nb}$  and  $\text{X} = \text{S}, \text{Se}$ , or  $\text{Te}$ ). TMTCs exhibit a wide range of structure-dependent transport properties, inspiring their application as high-pressure superconductors [24], charge density wave (CDW) materials [25, 26], and visible and infrared emitters [27, 28]. Unlike many 2D materials, TMTCs have in-plane anisotropy, which leads to axis-dependent strain responses [29]. The electronic band structures of TMTCs are quite resistant to stacking order when compared to those of 2D materials; this has been attributed to the electronic states near the band edge being localized to the internal transition metal-sulfur ( $\text{M-S}$ ) bonding direction [30].

The anisotropic relationships among bulk TMTc properties are well studied [30–35], but exploration of their intrinsic defect properties has been comparatively limited in scope [27, 36–39]. Recent DFT efforts to systematically characterize intrinsic defects in  $\text{TiS}_3$ , including S and Ti vacancies up to relatively high doping concentrations, revealed that these defects can contribute to *n*- or

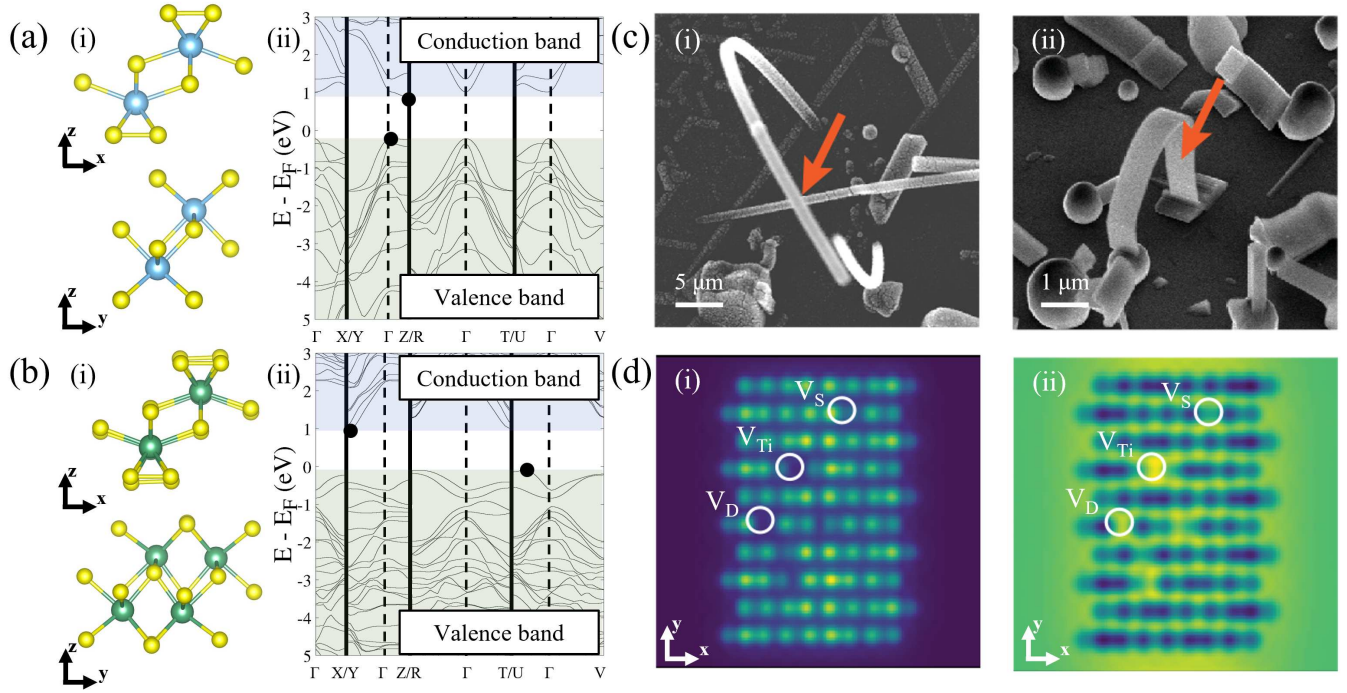


FIG. 1. Theoretical predictions of TMTC unit cell geometry (i) and electronic band structure (ii) for (a) TiS<sub>3</sub> and (b) NbS<sub>3</sub>. Band energies are plotted relative to the Fermi energy. (c) SEM images of bent (i) TiS<sub>3</sub> and (ii) NbS<sub>3</sub> nanowires (indicated by an orange arrow). (d) Simulated scanning transmission electron microscopy (STEM) images showing common intrinsic defects (V<sub>S</sub>: sulfur vacancy, V<sub>D</sub>: sulfur divacancy and V<sub>Ti</sub>: titanium vacancy) in TiS<sub>3</sub> nanowires in dark field (i) and bright field (ii) modes.

*p*-type conductivity and populate deep in-gap states [40]. The effect of S vacancies on exciton lifetimes in TiS<sub>3</sub> was also investigated to explain discrepancies in electron-hole recombination rates between experimental and theoretical studies [41]. Pairing time domain *ab initio* calculations and MD, it was found that S vacancies reduce the non-radiative recombination rate of excitons in TiS<sub>3</sub> by an order of magnitude. However, the accuracy of these efforts may be limited due to their use of PBE functionals [42], which are known to underestimate electronic band gaps and defect localization [43, 44].

Inspired by previous reports on strain engineering of defect-induced SPEs in 2D vdW materials and our recent synthesis of TiS<sub>3</sub> and NbS<sub>3</sub> nanowires (Figures 1(c,d)), we use first principles calculations to characterize the local structure of intrinsic chalcogen vacancies in TiS<sub>3</sub> and NbS<sub>3</sub> in response to uniaxial strain. We identify single-photon emitters with ZPLs ranging from 0.3 eV (mid-IR) to 0.6 eV (near-IR) with strain tunability of their ZPLs up to  $\pm 0.24$  eV. Additionally, we find that strain can also be used to induce a transition between singlet and triplet ground states in the sulfur vacancy (V<sub>S</sub>) defect in TiS<sub>3</sub> and the sulfur divacancy (V<sub>D</sub>) defect in NbS<sub>3</sub>. The inherent anisotropy and malleable optoelectronic properties of TMTC nanowires make them strong candidate materials for hosting entangled spin-photon defects with the additional advantage of strain-driven spin state tran-

sitions.

## METHODS

**Ab initio calculations.** All calculations were performed with the Vienna Ab Initio Simulation Package (VASP) [45, 46], which uses plane-wave basis sets following the projector augmented wave (PAW) method [47]. All geometry relaxations and electronic self-consistency calculations were converged to  $10^{-3}$  eV Å<sup>-1</sup> and  $10^{-10}$  eV, respectively. Sampling of the Brillouin zone for all structures was done at the  $\Gamma$  point with a cutoff energy of 650 eV.

TMTC supercells were constructed from respective unit cells (shown in Figures 1(a,b)) to host intrinsic S vacancy defects; the TiS<sub>3</sub> unit cell was extended to a  $4 \times 4 \times 1$  supercell (128 atoms), while the NbS<sub>3</sub> unit cell was extended to a  $3 \times 3 \times 1$  supercell (144 atoms). A vacuum layer of 15 Å was added in the  $z$ -direction to simulate TMTC monolayers. Pristine crystal supercells were geometry- and volume-relaxed using a screened hybrid functional. Contributions from DFT were calculated using a generalized gradient approximation [42] including vdW dispersion energy corrections calculated according to the zero-damping DFT-D3 method [48]. We find that the Heyd-Scuseria-Ernzerhof (HSE06) func-

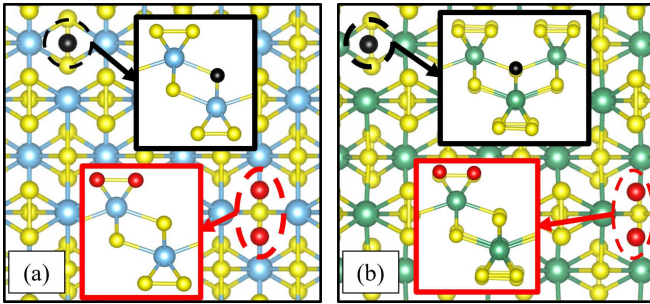


FIG. 2. Vacancy defects in (a)  $\text{TiS}_3$  and (b)  $\text{NbS}_3$ .  $V_S$  and  $V_D$  defects are shown in black and red, respectively.

tional [49] well reproduces the electronic band gaps of both pristine  $\text{TiS}_3$  and  $\text{NbS}_3$  crystal structures. Volume relaxation results in good agreement with experimental lattice parameters for  $\text{TiS}_3$  [50] but an overestimation of 1.1 % of the  $b$ -lattice parameter for  $\text{NbS}_3$  [51]. Because the band edges and defect levels are sensitive to small amounts of strain, we expect that straining the crystal structures relative to their volume-relaxed geometries will provide a better description of strain-dependent electronic, optical, and spin properties. Strains ranging from -3 % (compressive) to 3 % (tensile) were induced independently in both in-plane directions (denoted by  $\varepsilon_x$  and  $\varepsilon_y$ ) by adjusting the  $a$ -lattice and  $b$ -lattice parameters followed by geometry relaxation.

The anisotropy of TMTC crystals gives rise to chemically distinct S ion species within the unit cells of  $\text{TiS}_3$  and  $\text{NbS}_3$ . Single  $V_S$  and  $V_D$  defects were embedded within the TMTC supercell structures to elucidate strain-dependent defect properties. We denote  $V_S$  as a vacancy of an internal S atom and  $V_D$  as a pair of nearest-neighbor S vacancies that make up the short edge of the triangular prismatic polyhedral surface, as shown in Figure 2. Defect-embedded supercells were geometry relaxed and subjected to the same lattice straining method performed for pristine TMTC supercells. Formation energies of  $V_S$  and  $V_D$  defects were calculated according to:

$$E_f(\varepsilon_j) = E_{\text{defect}}(\varepsilon_j) - E_{\text{pristine}}(\varepsilon_j) + \sum \mu_i n_i ,$$

where  $E_f$  is the formation energy,  $E_{\text{defect}}$  is the total energy of the defective system,  $E_{\text{pristine}}$  is the total energy of the pristine crystal, and  $\varepsilon_j$  ( $j = x, y$ ) is the axis-dependent strain. Changes in the chemical potential are accounted for in the last term, where  $\mu_i$  and  $n_i$  are the chemical potential and number of the removed S ions, respectively. We also probe the electronic structures corresponding to the simple excitations of the in-gap defect states via the constrained occupation method [52]; optical properties of the corresponding excitations were calculated using VASPKIT [53].

**Synthesis and characterization of transition metal trichalcogenide nanowires.**  $\text{TiS}_3$  and  $\text{NbS}_3$  nanowires were synthesized by salt-assisted chemical vapor deposition. Details of the experimental setup and the syn-

thesis parameters can be found in previously published work [54]. Scanning Electron Microscopy (SEM) images were acquired by Helios 5 UC with 5-10 keV beam energy. Multi-slice simulations of scanning transmission electron microscopy (STEM) images were conducted using abTEM package [55] with the microscope conditions similar to the experimental parameters (electron energy of 200 keV and convergence angle of 25 mrad).

## RESULTS AND DISCUSSION

**Strain tuning of pristine nanowires.** Our *ab initio* calculations reveal that pristine  $\text{TiS}_3$  and  $\text{NbS}_3$  nanowires have axis-dependent responses to compressive and tensile strains. Electronic band structures of unstrained  $\text{TiS}_3$  and  $\text{NbS}_3$  are plotted in Figures 1(a,b). While the  $\text{TiS}_3$  band gap of 1.10 eV is in good agreement with literature [30, 50], we find that its band gap is indirect rather than direct. We predict the energy difference between the direct and indirect band gap to be only 0.016 eV, so it is likely that this discrepancy is due to slight symmetry breaking of the pristine  $\text{TiS}_3$  crystal in our approach.

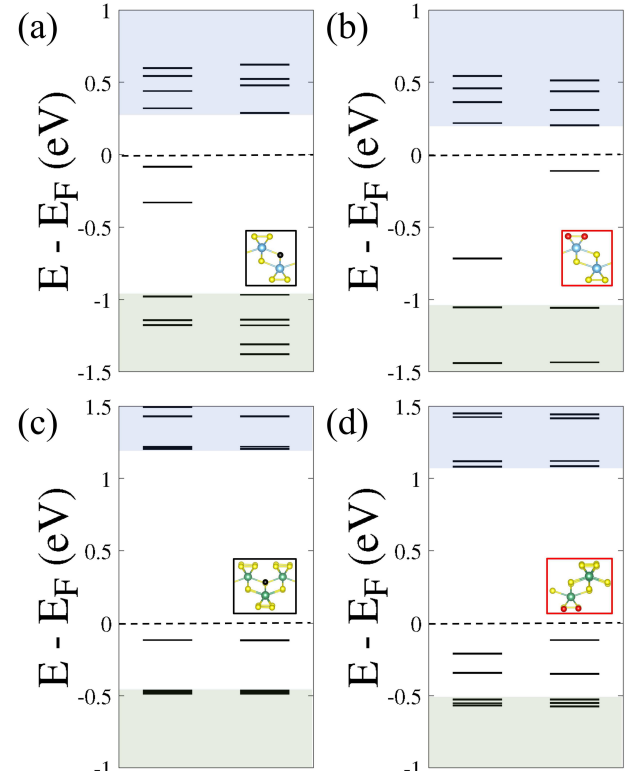


FIG. 3. Electronic structures of (a)  $V_S$ , (b)  $V_D$  in a  $4 \times 4 \times 1$   $\text{TiS}_3$  supercell, (c)  $V_S$ , (d)  $V_D$  in a  $3 \times 3 \times 1$   $\text{NbS}_3$  supercell, showing the conduction band (blue), valence band (green), localized defect states (black lines) plotted relative to the Fermi energy  $E_F$  (dashed line). Up/down spin channels are shown separately in the left/right columns of each panel.

We also reproduce the 1.22-eV indirect band gap of  $\text{NbS}_3$  [28].

Observation of many bent nanowires, both  $\text{TiS}_3$  and  $\text{NbS}_3$  (Figure 1(c)) in our growth indicates their mechanical flexibility. We next perform calculations on strain-response of the supercell structures and the electronic band structure.  $\text{TiS}_3$  and  $\text{NbS}_3$  supercells exhibit similar trends in response to anisotropic axial strains, both of which are plotted in Figure S.1 (see Supplementary Materials [56]). Compressive strains incur larger increases in the ground state energies of the pristine supercells, suggesting that the nanowire structures are more tolerant of tensile strains. These results are consistent with findings previously reported for 2D vdW materials, which can tolerate only small compressive strains before buckling out-of-plane [17]. Further, both compressive and tensile strain along the  $y$ -direction results in sharper increases in the ground state energies when compared to strain along the  $x$ -direction for both TMTc nanowires. The enhanced sensitivity to  $\varepsilon_y$  can be understood as a consequence of the strong covalent nature of M-S bonding in the  $y$ -direction, while M-S bonds in the  $x$ -direction of both  $\text{TiS}_3$  and  $\text{NbS}_3$  are comprised of weak covalent bonds and vdW interactions.

Similarly,  $\text{TiS}_3$  and  $\text{NbS}_3$  band gaps are more strongly dependent on  $\varepsilon_y$  than  $\varepsilon_x$ . Band gap responses to external strain (Figure S.1) are in good agreement with literature values [28, 31]. External strain in the  $y$ -direction results in a near-linear modulation of the band gap. We find that depending on the direction of strain, the band gaps of  $\text{TiS}_3$  and  $\text{NbS}_3$  can be increased or decreased by about 21 % and 15 % respectively, relative to the unstrained values. Wavefunction visualization of electronic states near the band edges (Figure S.2) confirms that M-S bonds are well hybridized along the  $y$ -direction in each TMTc crystal [30]. Band structure calculations from  $\varepsilon_y = -3\%$  to 3 % and  $\varepsilon_x = -3\%$  to 3 % are plotted in Figure S.3 [56]; we find that the positions of the valence band maximum (VBM) and conduction band minimum (CBM) are not sensitive to in-plane strain.

**Optically active sulfur vacancies.** Transition metal chalcogenides are prone to chalcogen (e.g., S) vacancies because of their high vapor pressure during the material growth. Our simulated scanning transmission electron microscopy (STEM) images (Figure 1(d)) show common intrinsic defects in  $\text{TiS}_3$  nanowires, including  $\text{V}_S$ ,  $\text{V}_D$  and  $\text{V}_{Ti}$ , which can be ambiguously identified. We perform calculations on the electronic, optical, and spin properties of selected intrinsic vacancy defects in quasi-1D  $\text{TiS}_3$  and  $\text{NbS}_3$  crystals using a hybrid-functional approach. We consider only  $\text{V}_S$  and  $\text{V}_D$  defects (Figure 2) in the dilute limit to mitigate the effects of self-interactions with periodic defect images that can occur for larger defect geometries and delocalized defect states.

The electronic structures of single  $\text{V}_S$  and  $\text{V}_D$  defects in  $\text{TiS}_3$  and  $\text{NbS}_3$  supercells are shown in Figure 3. Our

calculations reveal that both  $\text{V}_S$  and  $\text{V}_D$  defects possess in-gap states with optically bright electronic transitions. The computed defect properties, including formation energies, ZPLs, transition dipole moments (TDMs), and spin state are summarized in Table I. We find that incorporation of S vacancy defects slightly widens the electronic band gaps of both  $\text{TiS}_3$  and  $\text{NbS}_3$ , consistent with previously reported theoretical studies of S vacancies in  $\text{TiS}_3$  [39, 41]. This behavior is attributed to decreased hybridization between transition metal and S orbitals, which in turn pushes the highest occupied molecular orbital (HOMO) level downward.

We can compare the formation energies for S vacancies in  $\text{TiS}_3$  with previously reported calculations [39, 40]. Our calculations predict defect formation energies in  $\text{TiS}_3$  that are smaller than those reported by Iyikanat *et al*, likely in part due to calculation of ground state energies at different levels of theory and with different supercell sizes. We calculated defect energies using hybrid DFT and in a 4 x 4 x 1 supercell, while the previous work uses a smaller 3 x 3 x 1 supercell at the PBE level of theory, both of which may explain the predicted metallic behavior of their  $\text{V}_D$ -doped  $\text{TiS}_3$  system [57].

Vacancy defect levels lie higher in the band gap for  $\text{TiS}_3$  than for  $\text{NbS}_3$ .  $\text{V}_S$  and  $\text{V}_D$  defect states in  $\text{TiS}_3$  are somewhat hybridized with electronic states that populate the CBM, whereas analogous defects in  $\text{NbS}_3$  are hybridized with states that comprise the VBM. While  $\text{TiS}_3$  and  $\text{NbS}_3$  have similar band gaps, the optical transitions of intrinsic defects in  $\text{NbS}_3$  are associated with larger ZPL energies and thus emit closer to the telecom band. These emission properties are congruent with previous work detailing the near-IR emission of bulk  $\text{TiS}_3$  and  $\text{NbS}_3$  materials [27].

**Strain tunable defect spin states.** Similar to bulk TMTc properties, intrinsic vacancy defect properties in  $\text{TiS}_3$  and  $\text{NbS}_3$  can be modulated via application of an

TABLE I. Defect properties of intrinsic S vacancy defects in  $\text{TiS}_3$  and  $\text{NbS}_3$ . We report the optical transitions corresponding to the two highest in-gap states of each defect. Formation energy values are compared to those reported by Iyikanat *et al* [39].

Host material	Defect	$E_{(F)}^{\text{th}}$ (eV)	$E_{(F)}^{\text{Lit}}$ (eV)	S	$E_{ZPL}$ (eV)	TDM <sup>2</sup> (Debye <sup>2</sup> )
$\text{TiS}_3$	$\text{V}_S$	1.08	3.58	1	0.26	50.3
	$\text{V}_D$	1.62	8.48	0	0.31	18.2
	$\text{V}_S$	1.52	-	0	0.23	2.10
	$\text{V}_D$	2.02	-	0	0.23	6.02
$\text{NbS}_3$	$\text{V}_S$	1.52	-	0	0.61	0.12
	$\text{V}_D$	2.02	-	0	0.62	16.8
	$\text{V}_S$	1.52	-	0	0.60	0.60
					0.65	0.41

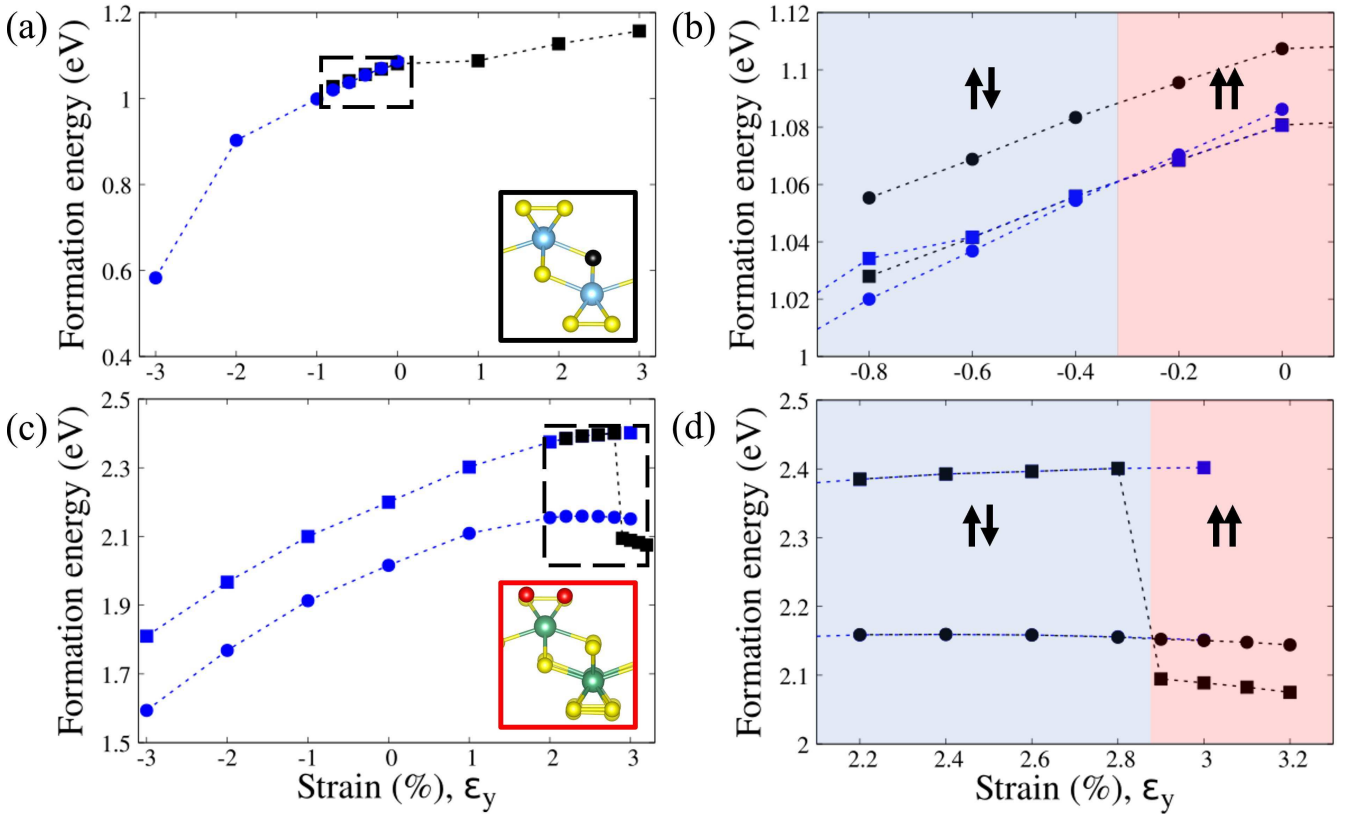


FIG. 4. Strain response of formation energies of intrinsic vacancy defects. Formation energy as a function of  $\varepsilon_y$  and the same curve with increased resolution are shown in (a) and (b), respectively, for  $V_S$  in  $TiS_3$  and (c) and (d) for  $V_D$  in  $NbS_3$ . Singlet ground states are plotted with circles, while square marks correspond to triplet ground states. Defect structural polymorphs are delineated with different color curves.

external strain. The  $V_S$  defect in  $TiS_3$  and the  $V_D$  defect in  $NbS_3$  were found to adopt strain-dependent structural polymorphs with associated transitions in their ground spin states. The formation energies of  $V_S$  in  $TiS_3$  and  $V_D$  in  $NbS_3$  as a function of strain in the  $y$ -direction are plotted in Figure 4; the remaining strain-formation energy plots are plotted in Figure S.4 [56].

We find that the formation energies of both  $V_S$  in  $TiS_3$  and  $V_D$  in  $NbS_3$  decrease as the crystal structures are compressed in the  $y$ -direction, shown in Figures 4(a,c). This trend can be attributed to the strain responses of pristine  $TiS_3$  and  $NbS_3$  crystals. Both pristine materials incur significant increases in ground state energies as they are compressed in the  $y$ -direction, while their defect systems show smaller increases in their ground state energies with increasing compressive strain. This can be interpreted as vacancy defects alleviating external compressive strains in both  $TiS_3$  and  $NbS_3$ . This relationship between defect formation energy and external strain in low-dimension materials has been reported on previously [17].

Our first principles calculations predict that the  $V_S$  defect in  $TiS_3$  has competing singlet and triplet ground states at low compressive strains from  $\varepsilon_y = -1\%$  to  $-0.2\%$ , as shown in Figures 4(a,b). For zero strain, the for-

mation energy of the triplet ground state lies  $\sim 0.03$  eV below that of the singlet, moving to lower energies for increasing tensile strain. At  $\varepsilon_y = -0.4\%$ , the formation energies of the singlet and triplet ground states flip, indicating that the singlet ground state may be induced through moderate compressive strain.

We have identified a similar transition for the  $V_D$  defect in  $NbS_3$ . Our calculations indicate that the ground state spin configuration of the  $V_D$  defect flips from a singlet to a triplet at a high tensile strain of  $\varepsilon_y = 2.9\%$ , as can be seen in Figures 4(c,d). Rather than a reversal of the singlet and triplet state formation energies (as is the case for the  $V_S$  defect in  $TiS_3$ ), hybrid DFT calculations show that the triplet state of  $V_D$  has two stable configurations, one of which is more stable than the singlet ground state at  $\varepsilon_y = 2.9\%$ . The energy difference between the singlet and triplet ground states at zero strain is about 0.18 eV, suggesting that the singlet state is considerably more stable in the absence of an external strain.

The defect wavefunctions of the strain-dependent ground states of  $V_S$  in  $TiS_3$  and  $V_D$  in  $NbS_3$  are shown in Figure 5 as well as the strain dependence of HOMO levels relative to the CBM. The singlet wavefunctions are well isolated to the nanowire growth axis but show

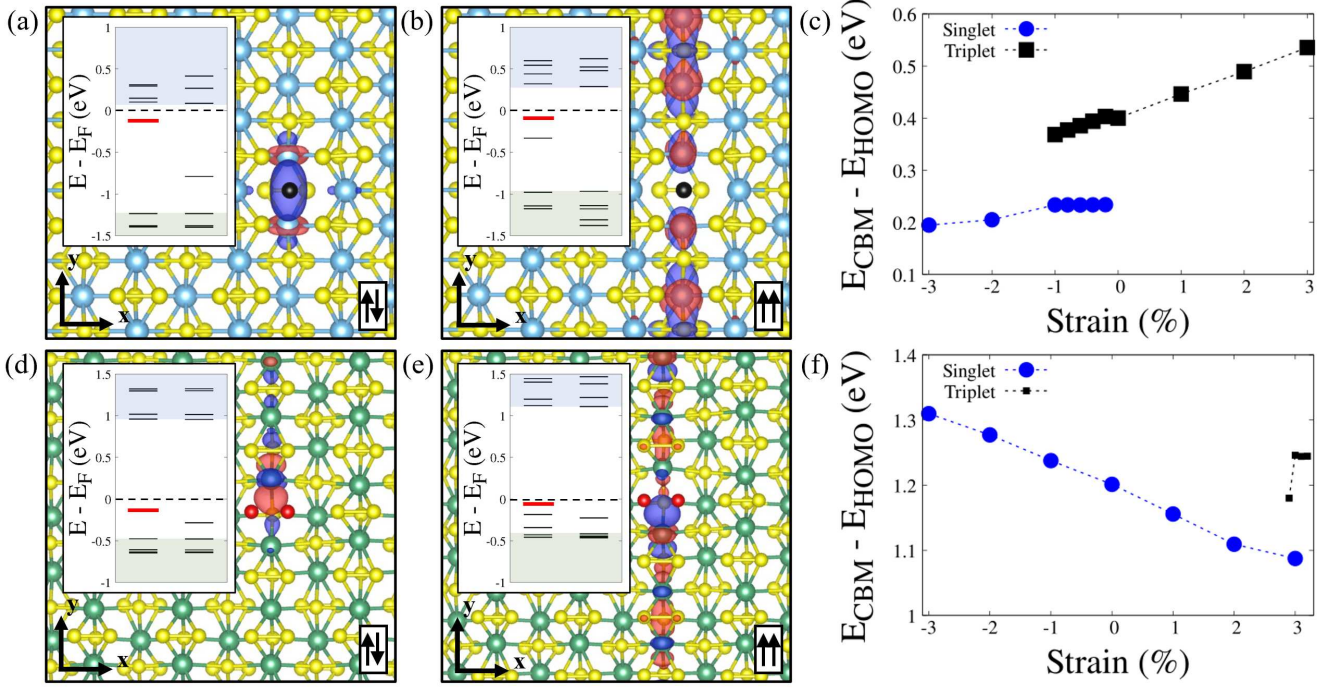


FIG. 5. Strain tunable spin states of  $V_S$  in  $TiS_3$  and  $V_D$  in  $NbS_3$ . (a) Spin singlet and (b) spin triplet state wavefunctions of  $V_S$  in  $TiS_3$  at  $\varepsilon_y = -0.4\%$  and (c) defect position of the HOMO level relative to the CBM. (d) Spin singlet and (e) spin triplet state wavefunctions of  $V_D$  in  $NbS_3$  at  $\varepsilon_y = 2.9\%$  and (f) defect position of the HOMO level relative to the CBM. The insets of (a), (b), (d), and (f) correspond to the defect electronic structures, following the same conventions described in 3. The HOMO levels that are plotted in (c) and (f) are indicated with red lines.

a large dispersion in that direction in the case of the spin triplet states (Figure 5(a,d)). Figure 5(c) shows how the position of the HOMO level of both the singlet and triplet state relative to the CBM in  $TiS_3$  increases as tensile strain is applied, consistent with the relationship established between  $\varepsilon_y$  and the electronic band gap. The electronic band gap of  $TiS_3$  closes by approximately 0.1 eV at  $\varepsilon_y = -1\%$ ; at the same compressive strain, the HOMO level is found to lie about 0.03 eV closer to the CBM relative to the uncompressed case. Thus, the defect comprises a somewhat shallow in-gap state that can hybridize with states at the CBM. The spin singlet state is favorable for  $\varepsilon_y \leq 0.4\%$  and has a ZPL of 0.26 eV.

The position of the spin triplet HOMO level relative to the CBM in  $NbS_3$  does not vary significantly at  $\varepsilon_y \geq 3\%$  (Figure 5(f)). However, the position of the spin singlet HOMO level has a span of about 0.21 eV across the range of compressive and tensile strains. In this same range, the band gap of  $NbS_3$  varies from 1.03 to 1.41 eV. These findings suggest that functionalization of spin-photon entangled qubits will require additional deformation to better isolate defect systems within the material band gaps [18]. The high-spin state achieved at  $\varepsilon_y \geq 2.9\%$  exhibits a ZPL of 0.83 eV (1500 nm).

Examination of defect wavefunctions in Figure 5(a, b, d, e) reveals that quasi-1D geometries of TMTC monolayers act to confine defect states to a uniaxial spread.

Specifically, the anisotropic bonding well localizes defect states to the  $y$ -direction, i.e., the predominately covalent bonding direction, similar to the hybridization of near-band edge states [30]. Unlike defects in 2D vdW materials that exhibit biaxial localization [7, 58], confinement of defect states to a single direction in TMTCs has two distinct advantages. The defect states are well localized along a single direction, which is ideal for QIS applications where indistinguishable single-photon emission is necessary for scalability. On the other hand, hybridization of defect states with bulk states make their properties sensitive to external stimuli (such as strains or twists [59]) that affect their electronic structures. Strategies to improve confinement of defect states in TMDCs are known to be necessary for overcoming hybridization with bulk states [18], so similar measures will likely be needed to tailor spectral properties of TMTC defects toward single-photon emission.

Our remaining strain tuning calculations (Figure S.4 [56]), including  $V_D$  in  $TiS_3$  and  $V_S$  in  $NbS_3$  at varied values of  $\varepsilon_x$  and  $\varepsilon_y$ , did not show transitions in their ground spin states. We previously discussed how strain in the  $x$ -direction has a more significant impact than strain in the  $y$ -direction on the electronic structures of TMTC nanowires (Fig. S.1 [56]). We similarly expect that the spin and optical properties of TMTC point defects will be more strongly perturbed by  $y$ -axis strain. Our calcula-

tions spotlight intrinsic vacancy defects in quasi-1D  $\text{TiS}_3$  and  $\text{NbS}_3$  nanowires as an attractive material platform for semiconductor qubits with tunable optical emission wavelengths and spin state toggling.

## CONCLUSION.

In summary, we present an *ab initio* analysis of the interplay between external, anisotropic strain and the physical behaviors of vacancy defects in quasi-1D  $\text{TiS}_3$  and  $\text{NbS}_3$  nanowires. We demonstrate that the anisotropic structures of TMTC nanowires make them interesting candidate materials for hosting spin-photon qubits. This anisotropy results in axis-dependent material responses to strain; the weak covalent bonding in the  $x$ -direction also acts to confine defect wavefunctions along the  $y$ -axis. By applying compressive and tensile strains in the  $y$ -direction, the band gaps of  $\text{TiS}_3$  and  $\text{Nb}_3$  are tunable by  $\pm 0.23$  eV and  $\pm 0.21$  eV, respectively. Additionally, we show that the  $V_S$  defect in  $\text{TiS}_3$  and the  $V_D$  defect in  $\text{NbS}_3$  can adopt competing defect configurations associated with spin state transitions. A modest compressive strain of  $\varepsilon_y = -0.4\%$  can shift the formation energy of  $V_S$  in  $\text{TiS}_3$  such that the singlet ground state becomes energetically preferred to its triplet ground state. This electronic rearrangement also exhibits a small decrease in the ZPL, with a drop from 0.31 eV to 0.26 eV. On the other hand, a large tensile strain of  $\varepsilon_y = 2.9\%$  was found to induce a triplet ground state in the  $V_D$  defect in  $\text{NbS}_3$ , with an increase in ZPL from 0.65 eV to 0.83 eV (1500 nm).

We note that the strains required to modulate the defect spin states (-0.4 % to 2.9 %) are attainable experimentally [60, 61]. It was shown that 1D vdW materials, such as  $\text{NbSe}_3$  and  $\text{TiS}_3$ , exhibit an enhanced Young's modulus (6-8 fold increase compared to the bulk modulus) when the nanowire diameter is below a certain threshold ( $\sim 50$ -80 nm). This is in line with our recent experimental work [54] in which several  $\text{TiS}_3$  and  $\text{NbS}_3$  nanowires synthesized by chemical vapor deposition, have a diameter less than 50 nm and support a high degree of bending (Figure 1(c)). Regarding the defect formation, as we discussed, S vacancies have been reported as very common defects in metal chalcogenides because of their high vapor pressure compared to those in transition metals. In the future work, in addition to introducing S defects via a bottom-up synthesis, we will explore energetic beam irradiation as a deterministic pathway to create S vacancies on demand. Our work paves the way to introduce 1D vdW materials, nanowires of transition metal trichalcogenides, as a tunable platform to host defect-induced spin defects for quantum communication and sensing.

**Supporting Information.** Additional details on the first principles calculations can be found in the Supple-

mentary Material.

## ACKNOWLEDGMENTS

The authors acknowledge Advanced Research Computing at Virginia Tech (arc.vt.edu) for providing computational resources and technical support, and NCFL for shared facilities. VI acknowledges support from the National Science Foundation Growing Convergence Research Award 2428507.

\* vivanov@vt.edu

- [1] M. R. Wasielewski, M. D. E. Forbes, N. L. Frank, K. Kowalski, G. D. Scholes, J. Yuen-Zhou, M. A. Baldo, D. E. Freedman, R. H. Goldsmith, T. Goodson, et al., *Nature Reviews Chemistry* **4**, 490 (2020), ISSN 2397-3358, URL <https://doi.org/10.1038/s41570-020-0200-5>.
- [2] S. L. Bayliss, D. W. Laorenza, P. J. Mintun, B. D. Kovos, D. E. Freedman, and D. D. Awschalom, *Science* **370**, 1309 (2020), URL <https://www.science.org/doi/abs/10.1126/science.abb9352>.
- [3] A. J. Landig, J. V. Koski, P. Scarlino, U. C. Mendes, A. Blais, C. Reichl, W. Wegscheider, A. Wallraff, K. Ensslin, and T. Ihn, *Nature* **560**, 179 (2018), ISSN 1476-4687, URL <https://doi.org/10.1038/s41586-018-0365-y>.
- [4] J. R. Weber, W. F. Koehl, J. B. Varley, A. Jantotti, B. B. Buckley, C. G. V. de Walle, and D. D. Awschalom, *Proceedings of the National Academy of Sciences* **107**, 8513 (2010), URL <https://www.pnas.org/doi/pdf/10.1073/pnas.1003052107>, URL <https://www.pnas.org/doi/abs/10.1073/pnas.1003052107>.
- [5] G. Burkard, T. D. Ladd, A. Pan, J. M. Nichol, and J. R. Petta, *Rev. Mod. Phys.* **95**, 025003 (2023), URL <https://link.aps.org/doi/10.1103/RevModPhys.95.025003>.
- [6] W. Redjem, A. Durand, T. Herzog, A. Benali, S. Pezzagna, J. Meijer, A. Y. Kuznetsov, H. S. Nguyen, S. Cueff, J.-M. Gérard, et al., *Nature Electronics* **3**, 738 (2020), ISSN 2520-1131, URL <https://doi.org/10.1038/s41928-020-00499-0>.
- [7] L. Zeng, S. Zhang, J. Meng, J. Chen, J. Jiang, Y. Shi, J. Huang, Z. Yin, J. Wu, and X. Zhang, *ACS Applied Materials & Interfaces* **16**, 24899 (2024), pMID: 38687622, URL <https://doi.org/10.1021/acsami.4c02601>.
- [8] Y. Guo, J. Li, R. Dou, H. Ye, and C. Gu, *Fundamental Research* (2024), ISSN 2667-3258, URL <https://www.sciencedirect.com/science/article/pii/S2667325824000426>.
- [9] S. Meesala, Y.-I. Sohn, B. Pingault, L. Shao, H. A. Atikian, J. Holzgrafe, M. Gündoğan, C. Stavrakas, A. Sipahigil, C. Chia, et al., *Phys. Rev. B* **97**, 205444 (2018), URL <https://link.aps.org/doi/10.1103/PhysRevB.97.205444>.
- [10] A. Ristori, M. Khouri, M. Salvalaglio, A. Filippatos, M. Amato, T. Herzog, J. Meijer, S. Pezzagna, D. Hannani, M. Bollani, et al., *Advanced*

Optical Materials **12**, 2301608 (2024), URL <https://advanced.onlinelibrary.wiley.com/doi/abs/10.1002/adom.202301608>.

[11] J. M. Brevoord, L. G. C. Wienhoven, N. Codreanu, T. Ishiguro, E. van Leeuwen, M. Iuliano, L. De Santis, C. Waas, H. K. C. Beukers, T. Turan, et al., Applied Physics Letters **126**, 174001 (2025), ISSN 0003-6951, URL <https://doi.org/10.1063/5.0251211>.

[12] B. Tissot, P. Udvarhelyi, A. Gali, and G. Burkard, Phys. Rev. B **109**, 054111 (2024), URL <https://link.aps.org/doi/10.1103/PhysRevB.109.054111>.

[13] K. S. Kim, Y. Zhao, H. Jang, S. Y. Lee, J. M. Kim, K. S. Kim, J.-H. Ahn, P. Kim, J.-Y. Choi, and B. H. Hong, Nature **457**, 706 (2009), ISSN 1476-4687, URL <https://doi.org/10.1038/nature07719>.

[14] S. Bertolazzi, J. Brivio, and A. Kis, ACS Nano **5**, 9703 (2011), ISSN 1936-0851, URL <https://doi.org/10.1021/nn203879f>.

[15] A. V. Tyurnina, D. A. Bandurin, E. Khestanova, V. G. Kravets, M. Koperski, F. Guinea, A. N. Grigorenko, A. K. Geim, and I. V. Grigorieva, ACS Photonics **6**, 516 (2019), URL <https://doi.org/10.1021/acspophotonics.8b01497>.

[16] H. J. Conley, B. Wang, J. I. Ziegler, R. F. J. Haglund, S. T. Pantelides, and K. I. Bolotin, Nano Letters **13**, 3626 (2013), pMID: 23819588, URL <https://doi.org/10.1021/nl4014748>.

[17] P. Santra, S. Ghaderzadeh, M. Ghorbani-Asl, H.-P. Komsa, E. Besley, and A. V. Krasheninnikov, npj 2D Materials and Applications **8**, 33 (2024), ISSN 2397-7132, URL <https://doi.org/10.1038/s41699-024-00472-x>.

[18] K. Parto, S. I. Azzam, K. Banerjee, and G. Moody, Nature Communications **12**, 3585 (2021), ISSN 2041-1723, URL <https://doi.org/10.1038/s41467-021-23709-5>.

[19] H.-P. Komsa, S. Kurasch, O. Lehtinen, U. Kaiser, and A. V. Krasheninnikov, Phys. Rev. B **88**, 035301 (2013), URL <https://link.aps.org/doi/10.1103/PhysRevB.88.035301>.

[20] H. L. Stern, Q. Gu, J. Jarman, S. Eizagirre Barker, N. Mendelson, D. Chugh, S. Schott, H. H. Tan, H. Sirringhaus, I. Aharonovich, et al., Nature Communications **13**, 618 (2022), ISSN 2041-1723, URL <https://doi.org/10.1038/s41467-022-28169-z>.

[21] S. Vaidya, X. Gao, S. Dikshit, I. Aharonovich, and T. Li, Advances in Physics: X **8**, 2206049 (2023), URL <https://doi.org/10.1080/23746149.2023.2206049>, URL <https://doi.org/10.1080/23746149.2023.2206049>.

[22] T. Yang, N. Mendelson, C. Li, A. Gottscholl, J. Scott, M. Kianinia, V. Dyakonov, M. Toth, and I. Aharonovich, Nanoscale **14**, 5239 (2022), URL <https://doi.org/10.1039/D1NR07919K>.

[23] X. Lyu, Q. Tan, L. Wu, C. Zhang, Z. Zhang, Z. Mu, J. Zúñiga-Pérez, H. Cai, and W. Gao, Nano Letters **22**, 6553 (2022), pMID: 35960708, URL <https://doi.org/10.1021/acs.nanolett.2c01722>, URL <https://doi.org/10.1021/acs.nanolett.2c01722>.

[24] B. Yue, W. Zhong, W. Deng, T. Wen, Y. Wang, Y. Yin, P. Shan, J.-T. Wang, X. Yu, and F. Hong, Journal of the American Chemical Society **145**, 1301 (2023), ISSN 0002-7863, URL <https://doi.org/10.1021/jacs.2c11184>.

[25] A. S. Semakin, I. R. Mukhamedshin, S. G. Zybtsev, and V. Y. Pokrovskii, JETP Letters **119**, 444 (2024), ISSN 1090-6487, URL <https://doi.org/10.1134/S0021364024600435>.

[26] S. G. Zybtsev, V. Y. Pokrovskii, V. F. Nasretdinova, S. V. Zaitsev-Zotov, V. V. Pavlovskiy, A. B. Odobesco, W. W. Pai, M.-W. Chu, Y. G. Lin, E. Zupanič, et al., Phys. Rev. B **95**, 035110 (2017), URL <https://link.aps.org/doi/10.1103/PhysRevB.95.035110>.

[27] A. Khatibi, R. H. Godiksen, S. B. Basuvalingam, D. Pellegriño, A. A. Bol, B. Shokri, and A. G. Curto, 2D Materials **7**, 015022 (2019), URL <https://doi.org/10.1088/2053-1583/ab57ef>.

[28] S. Conejeros, B. Guster, P. Alemany, J.-P. Pouget, and E. Canadell, Chemistry of Materials **33**, 5449 (2021), URL <https://doi.org/10.1021/acs.chemmater.1c01417>.

[29] M. Li, J. Dai, and X. C. Zeng, Nanoscale **7**, 15385 (2015), URL <https://dx.doi.org/10.1039/C5NR04505C>.

[30] J. Kang and L.-W. Wang, Phys. Chem. Chem. Phys. **18**, 14805 (2016), URL <https://dx.doi.org/10.1039/C6CP01125J>.

[31] F. Saiz and R. Rurrali, Nano Express **1**, 010026 (2020), URL <https://doi.org/10.1088/2632-959X/ab89ea>.

[32] H. Shu, Journal of Materials Science **57**, 3486 (2022), ISSN 1573-4803, URL <https://doi.org/10.1007/s10853-022-06884-8>.

[33] J. Zhang, C. Chen, Y. Wang, Y. Lu, H. Li, X. Hou, Y. Liang, L. Fang, D. Xiang, K. Zhang, et al., Frontiers of Physics **19**, 43203 (2024), ISSN 2095-0470, URL <https://doi.org/10.1007/s11467-023-1376-1>.

[34] C. K. Gan and K. T. E. Chua, Journal of Physics: Condensed Matter **31**, 265401 (2019), URL <https://doi.org/10.1088/1361-648X/ab13f7>.

[35] Y. Saeed, A. Kachmar, and M. Carignano, Journal of Physical Chemistry C **121**, 1399 (2017), ISSN 1932-7447, publisher Copyright: © 2016 American Chemical Society.

[36] Z. Tian, X. Guo, D. Wang, D. Sun, S. Zhang, K. Bu, W. Zhao, and F. Huang, Advanced Functional Materials **30**, 2001286 (2020), URL <https://advanced.onlinelibrary.wiley.com/doi/abs/10.1002/adfm.202001286>.

[37] E. V. Formo, J. A. Hachtel, Y. Ghafouri, M. A. Bloodgood, and T. T. Salguero, Chemistry of Materials **34**, 279 (2022), URL <https://doi.org/10.1021/acs.chemmater.1c03411>.

[38] H. Zheng, M. Zhu, J. Zhang, X. Du, and Y. Yan, RSC Adv. **6**, 55194 (2016), URL <https://dx.doi.org/10.1039/C6RA06486H>.

[39] F. Iyikanat, H. Sahin, R. T. Senger, and F. M. Peeters, The Journal of Physical Chemistry C **119**, 10709–10715 (2015), ISSN 1932-7455, URL <https://dx.doi.org/10.1021/acs.jpcc.5b01562>.

[40] G. Dongho-Nguimdo, E. Igumbor, E. Benecha, A. Raji, and E. Lombardi, Computational Condensed Matter **40**, e00947 (2024), ISSN 2352-2143, URL <https://www.sciencedirect.com/science/article/pii/S2352214324000698>.

[41] Y. Wei, Z. Zhou, and R. Long, The Journal of Physical Chemistry Letters **8**, 4522 (2017), pMID: 28876946, URL <https://doi.org/10.1021/acs.jpclett.7b02099>, URL <https://doi.org/10.1021/acs.jpclett.7b02099>.

[42] J. P. Perdew, Physica B: Condensed Matter **172**, 1 (1991), ISSN 0921-4526, URL <https://www.sciencedirect.com/science/article/pii/0921452691904098>.

[43] P. Borlido, J. Schmidt, A. W. Huran, F. Tran, M. A. L. Marques, and S. Botti, *npj Computational Materials* **6**, 96 (2020), ISSN 2057-3960, URL <https://doi.org/10.1038/s41524-020-00360-0>.

[44] P. Deák, B. Aradi, T. Frauenheim, E. Janzén, and A. Gali, *Phys. Rev. B* **81**, 153203 (2010), URL <https://link.aps.org/doi/10.1103/PhysRevB.81.153203>.

[45] G. Kresse and J. Hafner, *Phys. Rev. B* **47**, 558 (1993), URL <https://link.aps.org/doi/10.1103/PhysRevB.47.558>.

[46] G. Kresse and J. Furthmüller, *Phys. Rev. B* **54**, 11169 (1996), URL <https://link.aps.org/doi/10.1103/PhysRevB.54.11169>.

[47] P. E. Blochl, *Phys. Rev. B* **50**, 17953 (1994), URL <https://link.aps.org/doi/10.1103/PhysRevB.50.17953>.

[48] S. Grimme, J. Antony, S. Ehrlich, and H. Krieg, *The Journal of Chemical Physics* **132**, 154104 (2010), ISSN 0021-9606, URL <https://doi.org/10.1063/1.3382344>.

[49] J. Heyd, G. E. Scuseria, and M. Ernzerhof, *The Journal of Chemical Physics* **118**, 8207 (2003), ISSN 0021-9606, URL <https://doi.org/10.1063/1.1564060>.

[50] J. Dai and X. C. Zeng, *Angewandte Chemie International Edition* **54**, 7572 (2015), URL <https://onlinelibrary.wiley.com/doi/abs/10.1002/anie.201502107>.

[51] M. A. Bloodgood, P. Wei, E. Aytan, K. N. Bozhilov, A. A. Balandin, and T. T. Salguero, *APL Materials* **6**, 026602 (2017), ISSN 2166-532X, URL <https://doi.org/10.1063/1.5005813>.

[52] A. Gali, E. Janzén, P. Deák, G. Kresse, and E. Kaxiras, *Phys. Rev. Lett.* **103**, 186404 (2009), URL <https://link.aps.org/doi/10.1103/PhysRevLett.103.186404>.

[53] V. Wang, N. Xu, J.-C. Liu, G. Tang, and W.-T. Geng, Computer Physics Communications **267**, 108033 (2021), ISSN 0010-4655, URL <https://www.sciencedirect.com/science/article/pii/S0010465521001454>.

[54] T. Pham, K. Reidy, J. D. Thomsen, B. Wang, N. Deshmukh, M. A. Filler, and F. M. Ross, *Advanced Materials* **36**, 2309360 (2024), URL <https://advanced.onlinelibrary.wiley.com/doi/abs/10.1002/adma.202309360>.

[55] J. Madsen and T. Susi, *Open Research Europe* **1** (2021).

[56] The Supplemental Material at [URL will be inserted by publisher] contains further details about the first-principles calculations.

[57] B. Rana, M. P. Coons, and J. M. Herbert, *The Journal of Physical Chemistry Letters* **13**, 5275 (2022), pMID: 35674719, URL <https://doi.org/10.1021/acs.jpclett.2c01187>.

[58] Y. Ping and T. J. Smart, *Nature Computational Science* **1**, 646 (2021), ISSN 2662-8457, URL <https://doi.org/10.1038/s43588-021-00140-w>.

[59] P. Sutter and E. Sutter, *Accounts of Chemical Research* **56**, 3235 (2023), pMID: 37938893, URL <https://doi.org/10.1021/acs.accounts.3c00502>.

[60] C. Liu, C. Wu, X. Y. Tan, Y. Tao, Y. Zhang, D. Li, J. Yang, Q. Yan, and Y. Chen, *Nature Communications* **14**, 5597 (2023), ISSN 2041-1723, URL <https://doi.org/10.1038/s41467-023-41425-0>.

[61] L. Yang, Y. Tao, Y. Zhu, M. Akter, K. Wang, Z. Pan, Y. Zhao, Q. Zhang, Y.-Q. Xu, R. Chen, et al., *Nature Nanotechnology* **16**, 764 (2021), ISSN 1748-3395, URL <https://doi.org/10.1038/s41565-021-00884-6>.

Supporting information: *Ab initio* prediction of strain-tunable spin defects in quasi-1D  
TiS<sub>3</sub> and NbS<sub>3</sub> nanowires

Jordan Chapman<sup>1</sup>, Arindom Nag<sup>2</sup>, Thang Pham<sup>2</sup>, and Vsevolod Ivanov<sup>1,3,4</sup>

<sup>1</sup>Virginia Tech National Security Institute, Blacksburg, Virginia 24060, USA

<sup>2</sup>Department of Materials Science and Engineering, Blacksburg, Virginia 24061, USA

<sup>3</sup>Department of Physics, Virginia Tech, Blacksburg, Virginia 24061, USA

<sup>4</sup>Virginia Tech Center for Quantum Information Science and Engineering, Blacksburg, Virginia 24061,  
USA

**Corresponding author:** vivanov@vt.edu

- Figure S.1: Pristine TMTC nanowire response to in-plane strain.
- Figure S.2: Visualization of VBM and CBM wavefunctions.
- Figure S.3: Electronic band structures of TMTC nanowires at varied in-plane strains.
- Figure S.4: Formation energies of the sulfide vacancy (V<sub>S</sub>) and disulfide vacancy (V<sub>D</sub>) defects in TiS<sub>3</sub> and NbS<sub>3</sub>.

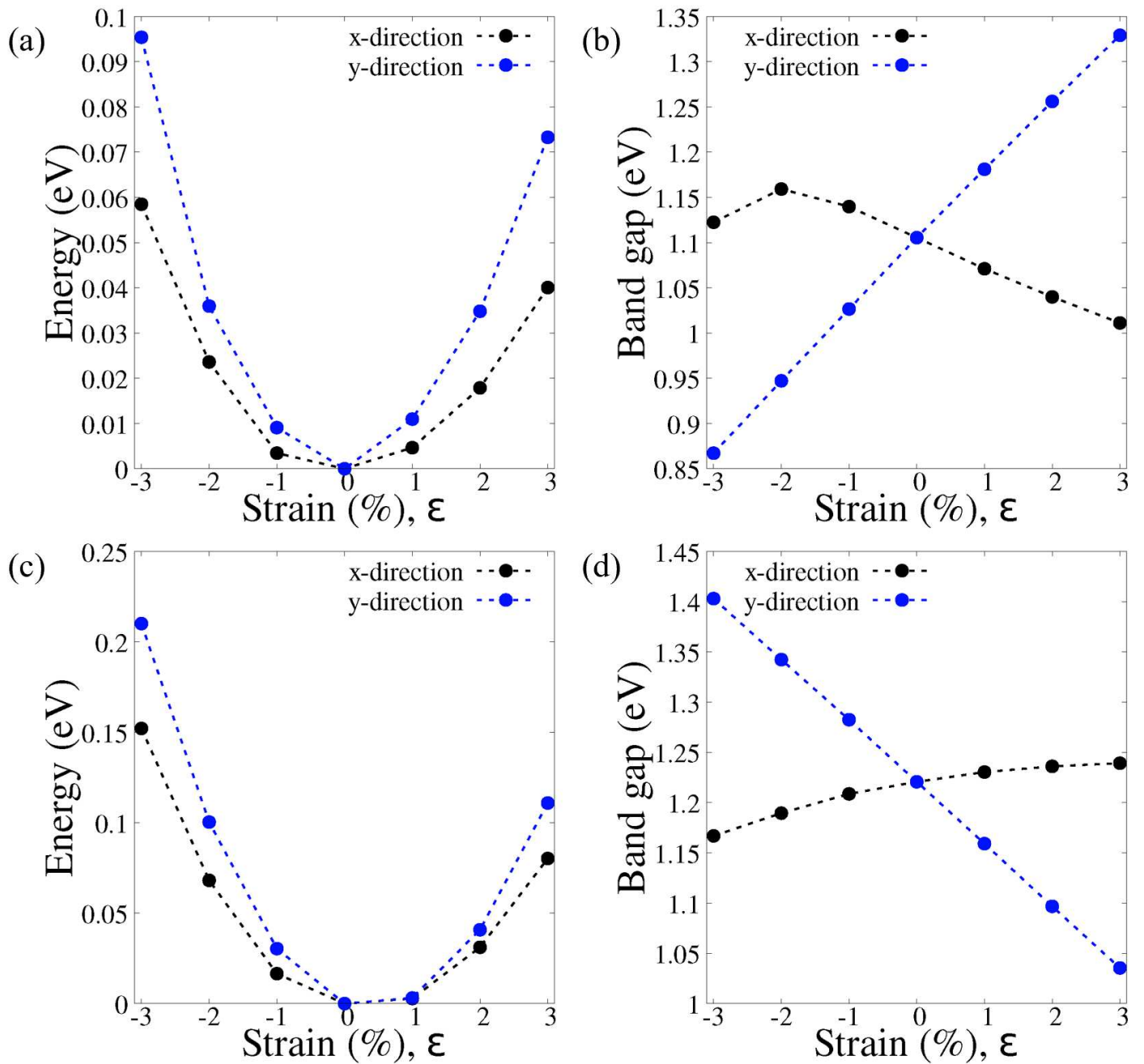


Figure S1: Pristine TMTC nanowire responses to in-plane strain. (a) Formation energy and (b) electronic band gap as a function of strain in the x- and y-directions for  $\text{TiS}_3$ . (c) Formation energy and (d) electronic band gap as a function of strain in the x- and y-directions for  $\text{NbS}_3$ .

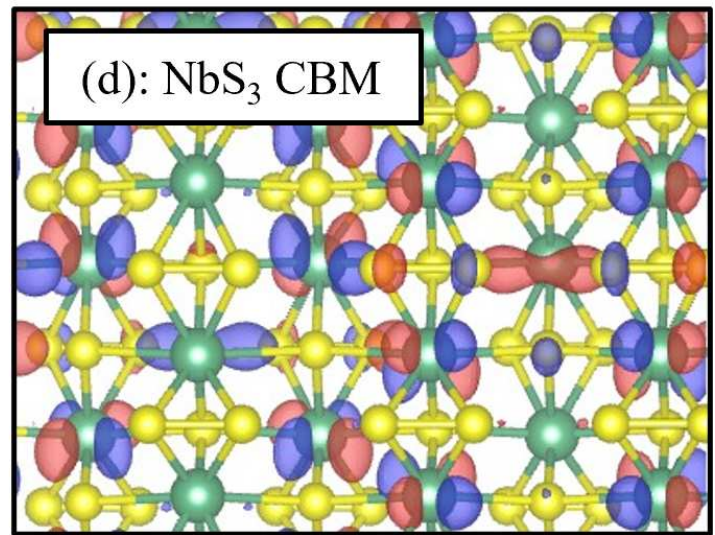
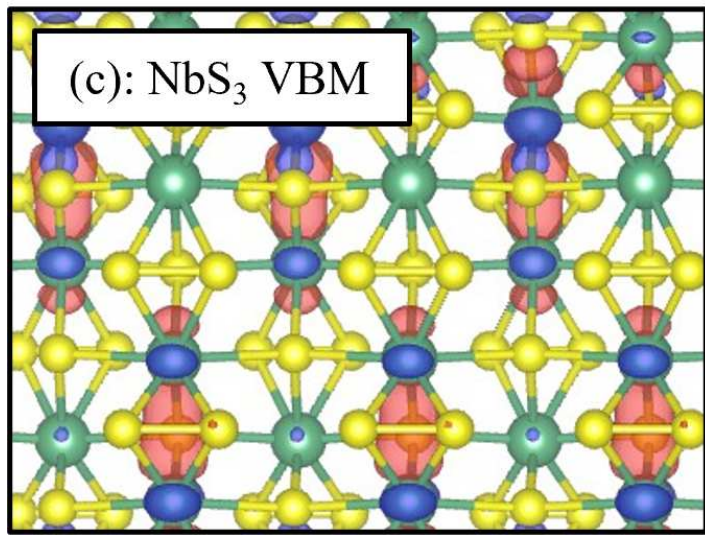
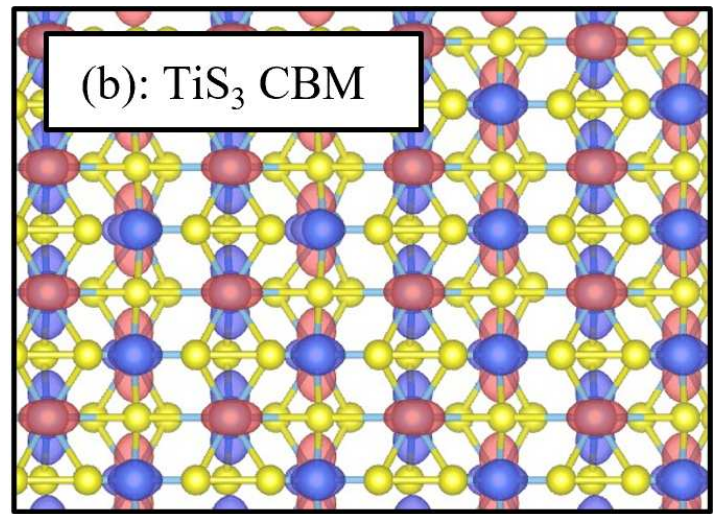
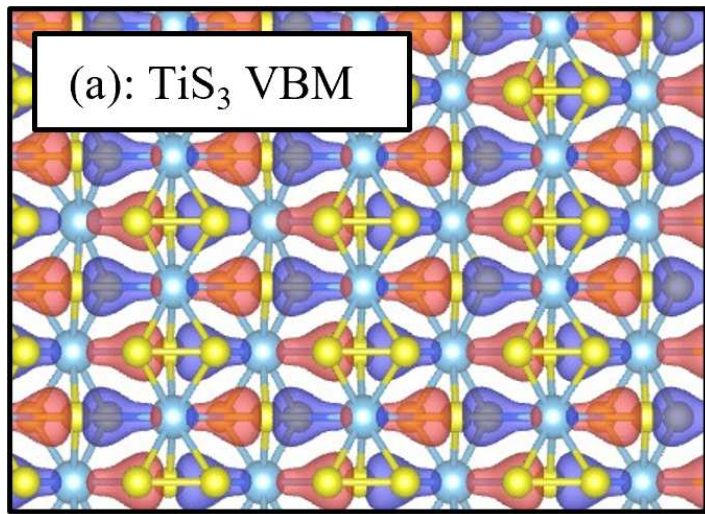


Figure S2: Visualization of wavefunctions population the valence band maximum (VBM) and conduction band minimum (CBM) of  $\text{TiS}_3$  and  $\text{NbS}_3$ .

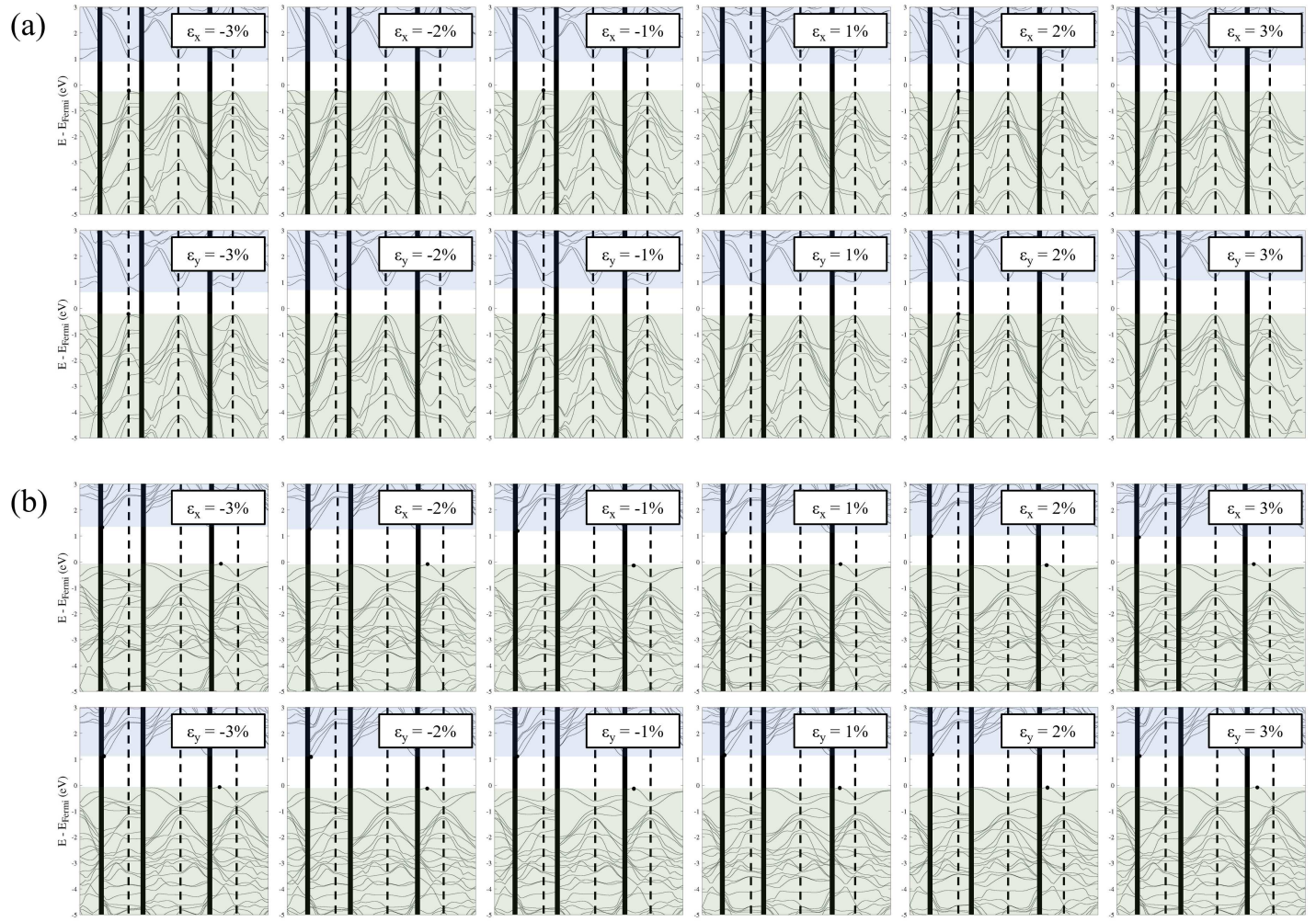


Figure S3: Electronic band structures of (a)  $\text{TiS}_3$  and (b)  $\text{NbS}_3$  at varied in-plane strains.

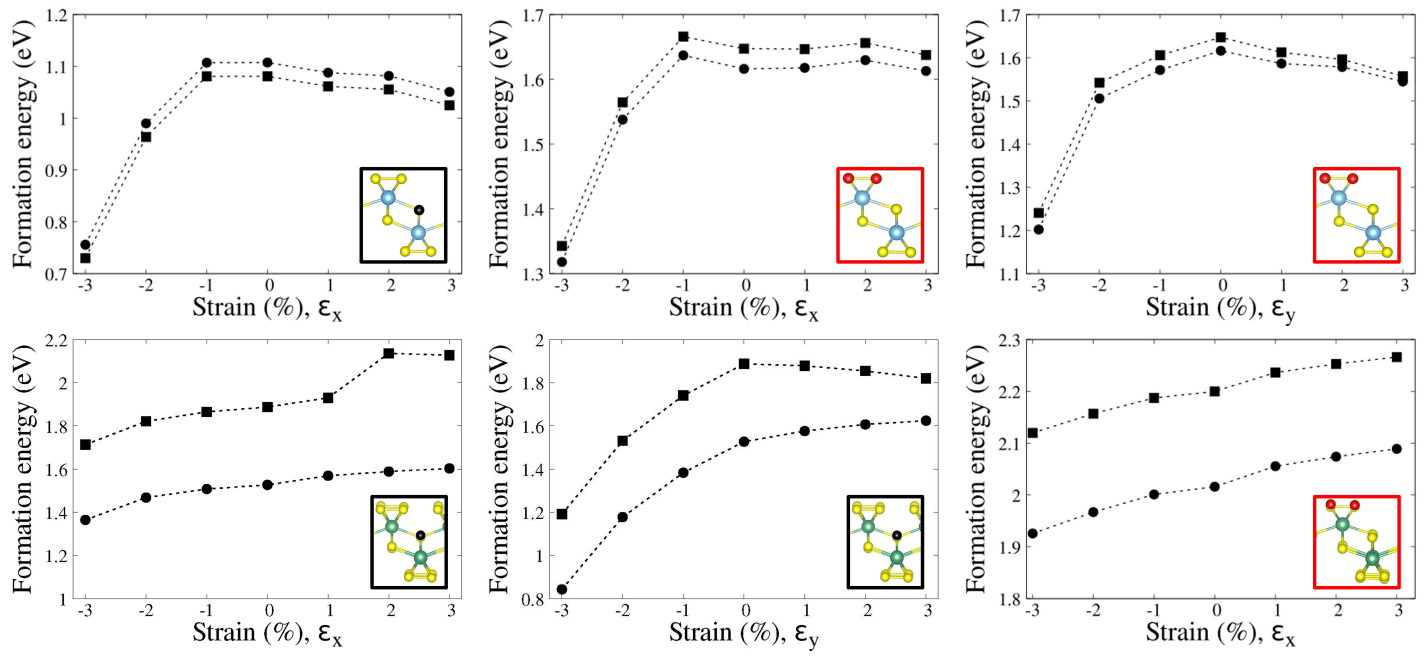


Figure S4: Formation energies of the sulfide vacancy (V<sub>S</sub>) and disulfide vacancy (V<sub>D</sub>) defects in TiS<sub>3</sub> and NbS<sub>3</sub>.